

**RESEARCH ARTICLE**

# Fully 3D Unrolled Magnetic Resonance Fingerprinting Reconstruction via Staged Pretraining and Implicit Gridding

Yonatan Urman<sup>1</sup>  | Mark Nishimura<sup>1</sup>  | Daniel Abraham<sup>2</sup>  | Xiaozhi Cao<sup>1,2</sup>  | Kawin Setsompop<sup>1,2</sup> 

<sup>1</sup>Electrical Engineering, Stanford University, California, USA

<sup>2</sup>Radiology, Stanford University, California, USA

**Correspondence**

Yonatan Urman: Email: [yurman@stanford.edu](mailto:yurman@stanford.edu)

## Abstract

**Purpose:** Magnetic Resonance Fingerprinting (MRF) enables rapid quantitative imaging, but high-resolution 3D reconstructions remain computationally expensive due to repeated NUFFTs, and the commonly used Locally Low Rank (LLR) regularization becomes ineffective at high acceleration. Learned 3D priors could address these limitations, but training them at scale is challenging due to memory and runtime constraints. This work proposes SPUR-iG, a fully 3D deep unrolled subspace reconstruction framework for efficient and scalable 3D MRF.

**Methods:** SPUR-iG leverages implicit GROG-based data consistency (DC), which grids non-Cartesian k-space using a learned kernel, enabling efficient FFT-based DC with minimal artifacts. To enable scalable 3D unrolled training, we introduce a staged training strategy that keeps computation tractable while progressively improving reconstruction quality. We evaluate the method on a large *in vivo* dataset, as well as on cross-vendor out-of-distribution data.

**Results:** At 1 mm isotropic resolution, SPUR-iG outperforms LLR and a state-of-the-art hybrid 2D-3D unrolled baseline in both subspace coefficient quality and  $T_1/T_2$  accuracy. Whole-brain reconstructions complete in under 15 seconds, providing up to a  $111\times$  speedup for 2-minute scans relative to LLR. Notably, 30-second SPUR-iG  $T_1$  maps match or exceed the accuracy of 2-minute LLR.

**Conclusion:** SPUR-iG introduces a fully 3D unrolled reconstruction framework for MRF that improves both reconstruction speed and accuracy, making high-resolution accelerated 3D MRF more practical for clinical and research use.

## KEYWORDS:

Deep Learning, Image reconstruction, Magnetic Resonance Fingerprinting, Quantitative MRI, Unrolled networks

## 1 | INTRODUCTION

Quantitative MRI (qMRI) measures intrinsic tissue properties such as  $T_1$  and  $T_2$ , making it less sensitive to acquisition conditions than conventional contrast-weighted imaging, and thereby enabling consistent comparisons across subjects, time points, and sites<sup>1</sup>. As a result, qMRI has shown promise in studying brain development<sup>2,3</sup>, and tracking subtle neurodegenerative changes<sup>4,5</sup>, among other applications<sup>6,7</sup>. However, qMRI acquisitions are typically slow since they require sampling the temporal signal evolution of each voxel rather than acquiring a single contrast-weighted snapshot.

Magnetic Resonance Fingerprinting (MRF)<sup>8</sup> is a qMRI technique that encodes tissue parameters through a sequence of varying flip angles (FA), repetition times (TR), and potentially other acquisition settings across  $N_{TR}$  time points. At each TR, an image is acquired using an incoherency-promoting trajectory (e.g., rotated spirals), producing artifacts that are spatially and temporally incoherent and thus reduce interference with tissue-specific signal evolutions. After reconstructing the time series of images, voxel-wise signal evolutions are matched to a dictionary of Bloch-simulated signals, linking tissue parameters to their expected dynamics and enabling parameter estimation.

While highly efficient to acquire, 3D MRF data is computationally demanding to reconstruct, especially at high resolutions<sup>9,10</sup>. For example, reconstructing an MRF acquisition of the whole brain with  $N_{TR} = 500$  at 1 mm isotropic resolution requires tens of gigabytes to store the time series alone. Moreover, the non-Cartesian reconstruction necessitates repeated non-uniform FFTs (NUFFTs), which can be particularly slow for large 3D problems.

Subspace reconstruction<sup>11,12,13</sup> reduces the computational load by approximating the signal dictionary with a low-rank subspace of size  $k \ll N_{TR}$ , thereby lowering dimensionality and implicitly regularizing the reconstruction. The resulting subspace coefficient maps provide a compact representation of the image's signal evolutions across TRs, which can be used to extract quantitative  $T_1$  and  $T_2$  maps. Beyond traditional parameter mapping, these coefficient maps capture rich signal information that facilitates additional downstream applications. These range from multi-compartment modeling<sup>14</sup>, which is particularly valuable at gray-white matter (GM/WM) boundaries<sup>15</sup>, to high-quality clinical contrast synthesis<sup>16,17</sup> by capturing signal components not typically described by Bloch-simulated dictionaries (e.g., magnetization transfer). These advantages motivate a focus on reconstructing accurate subspace coefficient maps that can serve as input for diverse

applications beyond conventional single-compartment parameter mapping.

Yet, for highly accelerated MRF, additional regularization beyond the subspace model is required. Locally Low Rank (LLR)<sup>18,19</sup> is widely used, enforcing low-rank structure within local patches, but it requires computationally expensive singular value decompositions (SVD)<sup>20</sup>. At even higher acceleration rates, such as acquisitions targeting 1 mm isotropic whole-brain mapping in under 2 minutes, LLR alone is insufficient to preserve reconstruction quality.

Broadly, achieving high-fidelity 3D MRF at this resolution and these acceleration factors is limited by two primary bottlenecks: (1) the reliance on handcrafted priors that lack the expressivity to resolve fine details under high undersampling, and (2) the computationally expensive NUFFTs and regularization operators, which substantially raise reconstruction time and memory usage at high resolutions.

Recent advances address parts of these problems. iGROG<sup>21,22</sup> enables efficient coil-based gridding of non-Cartesian data onto a Cartesian grid using an implicit neural representation (INR)<sup>23</sup> of the gridding kernel, replacing expensive NUFFTs with efficient FFTs at negligible quality loss. This reduces high-resolution MRF reconstruction times from roughly 30 minutes to around 4 minutes.

However, even with iGROG, reconstruction still relies on suboptimal LLR priors. To address this, state-of-the-art unrolled methods like SOTIP<sup>24</sup> utilize deep learning to incorporate learned priors, showing significant improvements in both quality and speed. These methods interleave 3D data-consistency (DC) steps with denoising; however, due to memory constraints, the denoising is applied slice-by-slice in 2D. Hence, this approach fails to exploit the inherently 3D nature of MRF acquisitions, which exhibit 3D artifacts and spatial correlations. Furthermore, to accelerate reconstruction, SOTIP employs NUFFTs with reduced kernel sizes and oversampling, introducing small artifacts that the denoiser must learn to remove.

To address these issues, we propose SPUR-iG (Staged Pretraining for Unrolled Reconstruction with iGROG), a fully 3D deep unrolled reconstruction framework<sup>25,26</sup>. Our approach combines efficient iGROG-based DC with a learned 3D prior and a staged training strategy that enables large-scale unrolled training. We first pretrain a standalone denoiser with extensive data augmentation, then train with a greedy per-unroll-iteration loss to reduce memory demands<sup>27</sup>, and finally fine-tune the full unrolled model using gradient checkpointing<sup>28</sup>. To further improve robustness, the denoiser takes as input both the image and the unroll iteration index, enabling

it to amortize performance across varying artifact and noise levels. Evaluated on 45 *in vivo* acquisitions with retrospective undersampling spanning acquisition times from 2 minutes down to 30 seconds, and including an example from an out-of-distribution scanner, our framework achieves whole-brain 1 mm isotropic reconstructions in under 15 s in all cases, while surpassing existing methods in quality.

The contributions of this work are as follows:

1. We present a *fully 3D* unrolled subspace reconstruction method for MRF that improves both the subspace coefficient map quality and quantitative accuracy compared with baseline methods.
2. We achieve 1 mm whole-brain subspace MRF reconstructions in under 15 seconds by combining efficient iGROG-based DC with a model-based 3D denoiser.
3. We develop a staged training strategy that enables large-scale 3D unrolled training on moderate hardware and validate it on a large *in vivo* dataset with diverse acceleration levels, including data from an out-of-distribution scanner vendor.

## 2 | METHODS

To enable fast and accurate MRF reconstruction, we build on the standard subspace formulation and address its limitations of suboptimal priors and long reconstruction times. We propose a fully 3D unrolled framework that integrates a learned prior with an efficient DC formulation, along with a staged training strategy that makes large-scale training feasible within a reasonable compute and time budget. We begin by reviewing MRF acquisition and the subspace model, followed by unrolled reconstruction, and then present the details of our proposed method and evaluation pipeline. An overview of our approach is illustrated in Fig. 1.

### 2.1 | MRF Subspace Reconstruction

MRF consists of a sequence of  $N_{\text{TR}}$  acquisitions with varying excitation parameters (e.g., FAs), producing a time series of images  $\mathbf{x} \in \mathbb{C}^{N_{\text{TR}} \times N_v}$ , where  $N_v$  denotes the number of voxels in the volume. The excitation schedule is typically designed to maximize separability between tissue parameter pairs ( $T_1, T_2$ ), and reconstruction proceeds in two stages: (1) recovery of the time series  $\hat{\mathbf{x}}$  from undersampled k-space data, and (2) voxel-wise parameter estimation via dictionary matching, where

the temporal signal evolution is compared to a precomputed dictionary, and quantitative maps are obtained by selecting the entry with maximum cosine similarity.

Directly reconstructing the full time series  $\mathbf{x}$  is computationally intensive and ill-posed due to its high dimensionality and the heavy undersampling used in MRF. This can be mitigated by exploiting temporal redundancy and projecting the data onto a low-dimensional subspace  $\Phi \in \mathbb{C}^{N_{\text{TR}} \times k}$  ( $k \ll N_{\text{TR}}$ ) spanned by the top  $k$  singular vectors of the MRF dictionary. The time series is then approximated as  $\mathbf{x} \approx \Phi \boldsymbol{\alpha}$ , where  $\boldsymbol{\alpha} \in \mathbb{C}^{k \times N_v}$  are the subspace coefficient maps. We define the forward operator acting on  $\boldsymbol{\alpha}$  as  $\mathcal{A} = \mathcal{F}_u \mathbf{S} \Phi$ , with  $\mathbf{S}$  the coil sensitivities and  $\mathcal{F}_u$  the undersampled Fourier operator. Since  $\mathcal{F}_u \mathbf{S}$  acts on the spatial domain and  $\Phi$  on the temporal domain, these operators commute, allowing the costly  $\mathcal{F}_u \mathbf{S}$  to be applied directly in the reduced  $k$ -dimensional space.

At high acceleration, however, the subspace model alone is insufficient, and the reconstruction problem is typically augmented with an LLR prior, leading to

$$\hat{\boldsymbol{\alpha}} = \arg \min_{\boldsymbol{\alpha}} \|\mathcal{A}(\boldsymbol{\alpha}) - \mathbf{b}\|_2^2 + \lambda \text{LLR}(\boldsymbol{\alpha}), \quad (1)$$

where  $\mathbf{b}$  are k-space measurements and  $\text{LLR}(\boldsymbol{\alpha})$  enforces low-rank structure within local spatial patches of the coefficient maps.

### 2.2 | Unrolled Reconstruction

Equation (1) is commonly solved using accelerated proximal algorithms such as FISTA<sup>29</sup>, which alternate between DC updates and proximal steps. However, at high acceleration rates, LLR regularization becomes insufficient to constrain the undersampled problem, and in addition, its proximal operator requires repeated SVDs of local patches, making it computationally expensive.

Unrolled reconstruction addresses these issues by replacing the proximal operator with a learned denoiser, yielding the update scheme

$$\boldsymbol{\alpha}_{\frac{1}{2}}^{(i+1)} = \boldsymbol{\alpha}^{(i)} - \mu_i \mathcal{A}^H (\mathcal{A} \boldsymbol{\alpha}^{(i)} - \mathbf{b}), \quad (\text{DC step}) \quad (2)$$

$$\boldsymbol{\alpha}^{(i+1)} = f_{\boldsymbol{\theta}} \left( \boldsymbol{\alpha}_{\frac{1}{2}}^{(i+1)} \right), \quad (\text{learned prior}) \quad (3)$$

where  $f_{\boldsymbol{\theta}}$  is a deep learning-based denoiser and  $\mu_i$  are learnable step sizes. By unrolling this computation for a fixed number of steps,  $f_{\boldsymbol{\theta}}$  can be trained to recover clean images from undersampled inputs, enabling it to learn rich image statistics that surpass hand-crafted priors.

## Inference

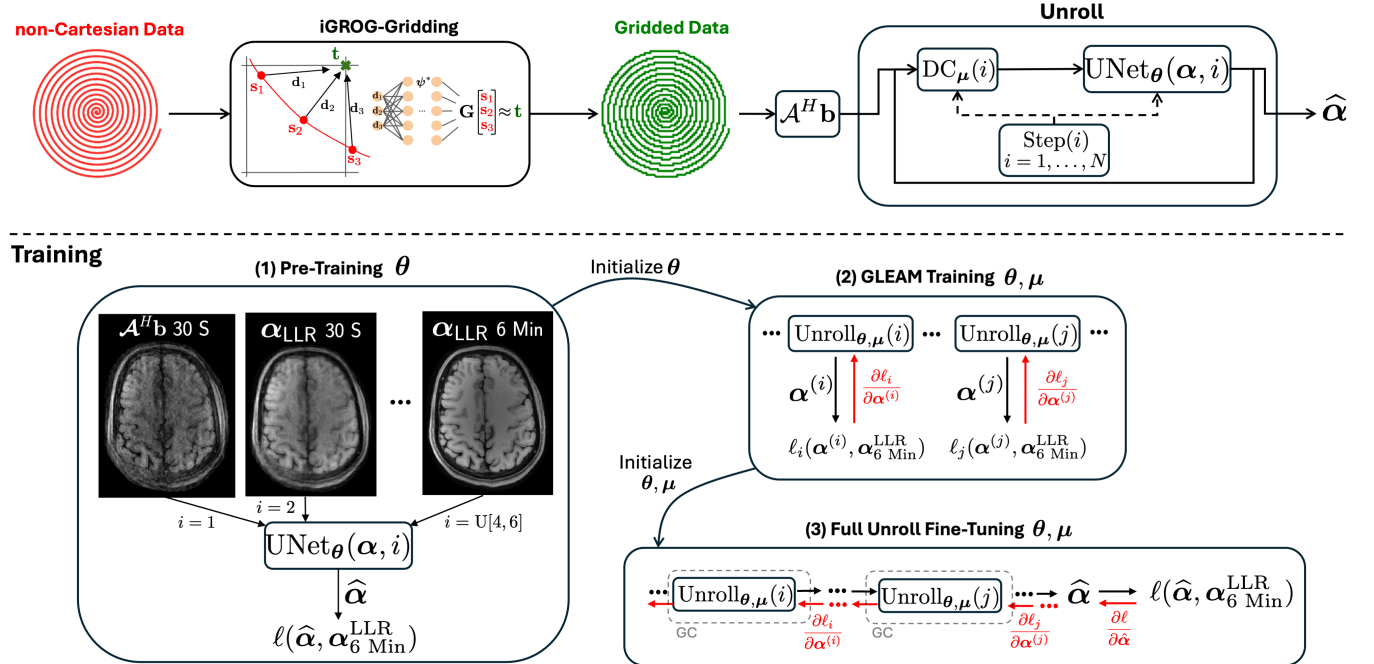


**FIGURE 1** Illustration of inference (top) and training (bottom) pipelines of SPUR-iG. During inference, iGROG grids the non-Cartesian data onto a Cartesian grid using an implicit kernel representation learned from the calibration region. The gridded k-space is then passed to the unrolled reconstruction, initialized with  $\mathcal{A}^H \mathbf{b}$ . Reconstruction proceeds for  $N$  unroll iterations, each alternating between a DC update with a learnable step size  $\mu_i$  and a step-conditioned denoiser. Training is performed in three stages: (1) a step-conditioned UNet is pretrained on inputs with varying artifact levels, using a heuristic mapping between input type and unroll step to promote robustness across noise/artifact conditions; (2) the pretrained UNet initializes GLEAM-style training, where losses are computed and backpropagated after each unroll iteration, detaching subsequent steps; and (3) full unrolled training, initialized from stage (2), fine-tunes the model under the exact inference setting, with gradient checkpointing (GC) across DC and denoising steps to reduce memory consumption.

## 2.3 | SPUR-iG Reconstruction

In large-scale 3D non-Cartesian settings, unrolled methods face two key challenges: (1) DC updates remain slow, as evaluating  $\mathcal{A}^H \mathcal{A}(\cdot)$  in (2) requires repeated NUFFTs, and (2) training fully 3D unrolled networks is memory-intensive, since the entire unrolled computation graph must be stored for backpropagation. We address these challenges with an efficient DC implementation and a scalable, progressive training framework.

### 2.3.1 | Efficient Data Consistency via iGROG

The main cost in (2) arises from evaluating  $\mathcal{A}^H \mathcal{A}(\cdot)$ , which relies on NUFFTs. To accelerate this step, we use iGROG, which learns an INR of the gridding kernel. Using calibration data, the INR is trained to map  $n$  offset vectors  $\mathbf{d}_1, \dots, \mathbf{d}_n$ , corresponding to displacements between non-Cartesian samples and a target Cartesian grid point, to a kernel  $G_{\psi^*}(\mathbf{d}_1, \dots, \mathbf{d}_n)$ . For each target

grid location, nearby source samples are selected, the kernel is evaluated at their relative displacements, and the resulting weights are used to compute the target k-space value. This enables GRAPPA-like<sup>30</sup> interpolation and, through the use of an INR, generalizes across the diverse orientations encountered in the trajectory. This allows us to first grid the non-Cartesian data onto a Cartesian grid, after which NUFFTs can be replaced by efficient FFTs. The upper left part of Fig. 1 illustrates this process.

The approach provides flexibility to trade off accuracy and noise amplification against speed. By using an oversampled grid, interpolation quality improves (since the interpolation distances are smaller), but reconstruction time increases. In our experiments, we used a  $\times 1.5$  oversampling ratio with 5 input points per interpolation, achieving high-quality reconstructions while retaining substantial speed-ups. The INR training is fast (under 25 s) and can be performed during MRF acquisition immediately after calibration data is acquired. Once trained, gridding the full dataset is also efficient (under

3 s), yielding data on a Cartesian grid for subsequent FFT-based DC updates.

### 2.3.2 | Efficient Training of a 3D Unrolled Network

For  $f_{\theta}$  in (3), we use a fully 3D UNet<sup>31</sup>, which enables the model to capture volumetric context and learn an effective unrolled denoising strategy. To improve data efficiency, weights are shared across unroll iterations, and FiLM-based<sup>32</sup> conditioning is introduced on the iteration index, i.e.,  $f_{\theta}(\alpha, i)$ . This conditioning enables the network to adapt its behavior across unroll steps, improving robustness by amortizing training over different noise and artifact regimes, similar to time conditioning in diffusion models<sup>33,34</sup>.

To enable training of a 3D unrolled network in the challenging MRF reconstruction setting, we adopt a progressive three-stage strategy, illustrated in the lower part of Fig. 1. This strategy consists of the following stages:

1. **Denoiser pretraining:** We begin by pretraining a standalone, iteration-conditioned 3D UNet on a diverse set of inputs, where the model is trained to recover clean images from noisy, undersampled inputs. To obtain a robust initialization for subsequent stages, we expose the network to a wide range of artifact and noise levels at its input, including zero-filled ( $\mathcal{A}^H \mathbf{b}$ ) and LLR-based reconstructions from scans with different acquisition durations (30 s, 1 min, 2 min, and 6 min, denoted  $\alpha_{\text{LLR}}^{\text{30s}}, \dots, \alpha_{\text{LLR}}^{\text{6min}}$ ). Since the UNet is iteration-conditioned, but this stage does not involve actual unrolling and therefore has no natural iteration index, we assign heuristic pseudo-iteration indices to each input type. Specifically,  $\mathcal{A}^H \mathbf{b}$  is paired with index 1, corresponding to the initialization of unrolled reconstruction, while reconstructions with increasing acquisition durations are mapped to higher indices (e.g.,  $\alpha_{\text{LLR}}^{\text{30s}} \rightarrow 2$ ). Because this stage does not involve unrolling or DC updates, we can efficiently apply extensive data augmentation, including random rotations, translations, and scaling. At the end of this stage, the network provides a well-initialized denoising prior that generalizes across a range of artifact levels and incorporates a notion of the unroll iteration index.

2. **Greedy unrolled training (GLEAM):** Starting from the pretrained weights, we train the unrolled network using a greedy scheme<sup>27</sup>, in which the loss is backpropagated through only a single unroll iteration at a time, after which the computation graph is detached. This avoids storing the full unrolled

graph, which would otherwise exceed typical GPU memory. Since the *final* output of the unrolled process is of primary interest, we assign geometrically increasing loss weights across iterations, emphasizing later steps while allowing greater flexibility in earlier ones. Importantly, this stage resolves the input distribution mismatch introduced during prior pretraining: while the denoiser from Stage 1 is trained on reconstructed images with different artifacts levels, during unrolled inference its true inputs are the intermediate outputs of preceding iterations. By the end of this stage, we obtain a fully unrolled model that achieves high reconstruction quality, with faster training convergence and improved performance due to the informed initialization.

3. **Final fine-tuning:** We finally fine-tune the model using full unrolled training, initialized from the GLEAM weights. In contrast to GLEAM, where losses applied at intermediate iterations may not fully align with optimal final reconstruction quality, this stage directly optimizes the denoiser with respect to the final output, thereby correcting this mismatch. Since full unrolled training is memory-intensive, we employ gradient checkpointing across both DC and denoising steps to reduce memory usage. Although each update in this stage is slow, the GLEAM-based initialization enables convergence in relatively few training iterations.

Collectively, these stages enable efficient large-scale training by progressively mitigating the limitations of each preceding stage, while circumventing the need to train a fully 3D unrolled model from scratch, which would otherwise be prohibitively compute expensive and slow. This process ultimately yields a high-quality, fully 3D unrolled reconstruction model. We refer to the resulting framework as **SPUR-iG**, introduced in Section 1. Code and trained models will be made publicly available upon publication.

### 2.4 | Dataset

We used a FISP-MRF sequence with a 3D Spiral Projection Imaging (SPI) acquisition<sup>35</sup>, beginning with an inversion pulse (TI = 20 ms) followed by  $N_{\text{TR}} = 500$  TRs (TE = 1.7 ms, TR = 12.5 ms). Each block of 500 TRs was extended by 40 additional TRs to acquire a low-resolution (4 mm isotropic) navigator for motion estimation<sup>36</sup>. The combined 540 TRs form an acquisition group with a total duration of 7.9 s, including a 1.2 s resting delay between groups to enable  $M_z$  recovery. Multiple groups are acquired using different spiral

projection interleaves and rotations to build up sufficient k-space encoding per TR position, with sampling patterns optimized for k-space coverage and incoherent aliasing using Tiny Golden-Angle Shuffling (TGAS)<sup>9</sup>. The acquisition resolution was 1 mm isotropic with a 220 mm  $\times$  220 mm  $\times$  220 mm field of view. Two tailored dummy-scan groups (16 s) were acquired at the start for  $B_1$  estimation<sup>37</sup>, and to enable steady-state signal to be reached prior to MRF acquisition.

Following TGAS<sup>9</sup>, we define an  $R = 1$  acquisition as 50 groups (including the two dummy groups), corresponding to a total scan time of 6 min 38 s. We considered undersampling factors of  $R = 3, 6$ , and 12, yielding scan times of 2 min 23 s, 1 min 19 s, and 47 s, respectively. For reporting, we use the raw MRF acquisition time (excluding the fixed dummy-group overhead), which we denote as 6 min, 2 min, 1 min, and 30 s for convenience. Practical strategies to bypass the need for these dummy groups are discussed in Section 4.1. All scans were coil-compressed to 10 virtual coils, and coil sensitivity maps were estimated using ESPiRiT<sup>38</sup>.

The dataset comprised 44 in vivo subjects scanned on a 3T GE system, with 36 used for training, 4 for validation, and 4 for testing. To assess cross-vendor generalization, we additionally evaluated our method on a subject scanned on a 3T Siemens system. For all subjects, motion was corrected in k-space using navigator data<sup>36</sup>. The  $R = 1$  acquisition was reconstructed using subspace reconstruction with light LLR regularization via FISTA and served as the training target. Quantitative maps were subsequently estimated using a  $B_1$ -corrected dictionary to mitigate systematic  $T_2$  bias<sup>39</sup>.

To improve numerical stability in SPUR-iG, which performs joint denoising across subspace coefficient maps, we do not directly use the raw SVD basis  $\Phi$  derived from the MRF signal dictionary, as later components contain substantially less energy. Instead, we apply basis balancing<sup>10</sup> by performing a discrete Fourier transform along the subspace dimension,  $\tilde{\Phi} = \mathbf{F}_k(\Phi)$ , where  $\mathbf{F}_k$  denotes a unitary DFT of length  $k$ . Since  $\mathbf{F}_k$  is orthonormal, this transformation is invertible and leaves the reconstruction solution unchanged, while redistributing energy more evenly across coefficients and thereby stabilizing the training of the learned denoisers. For fair comparison, the balanced basis was also used for all baseline methods.

Finally, we synthesized MPRAGE images from the  $R = 1$  quantitative maps using Bloch simulations and used them to obtain segmentation masks with FreeSurfer<sup>40</sup>. These masks were then used to apply region-specific loss weighting during model training.

All human data were acquired with informed consent under protocols approved by the local institutional review board.

## 2.5 | Evaluation

We evaluated our approach on the held-out test set using retrospectively undersampled acquisitions of 2 min, 1 min, and 30 s. Evaluation considered both the reconstruction quality of the subspace coefficient maps and the resulting quantitative  $T_1/T_2$  maps, obtained by voxel-wise dictionary matching with  $B_1$ -corrected dictionaries. In addition, we performed ablation studies to analyze the contribution of different components of our framework.

We benchmarked against two baselines:

1. **LLR:** Subspace reconstruction with FISTA and LLR regularization, where the regularization weight was tuned on the validation set separately for each scan duration to minimize  $T_1/T_2$  error in WM and GM. The number of iterations was set to 40, ensuring convergence of the loss.
2. **Hybrid 2D/3D:** Inspired by the state-of-the-art SOTIP<sup>24</sup>, this baseline alternates 3D DC updates with axial slice-wise 2D denoising. For a fair comparison, we train this model using the same progressive procedure. Unlike SPUR-iG, the denoiser here is a 2D UNet applied independently to each slice at every unroll iteration, with the 3D volume subsequently formed by stacking the denoised slices. To control for model capacity, we set the initial number of UNet filters such that both this model and SPUR-iG saturated the memory of a single NVIDIA A6000 GPU (48 GB) during fine-tuning.

Separate models were trained for each scan duration. For the unrolled models, we used six unroll iterations. Additional implementation details are provided in Appendix A.

## 3 | RESULTS

### 3.1 | Coefficient Reconstruction

Table 1 shows the PSNR and SSIM for the five balanced subspace coefficients across scan durations and reconstruction methods. SPUR-iG consistently achieves higher PSNR and SSIM compared to both LLR and the hybrid 2D/3D method, with performance gaps widening as scan duration decreases. Statistical testing confirms that our method outperforms both baselines with  $p < 0.001$  across all metrics and subspace dimensions.

Method	PSNR (dB) ↑					SSIM ↑					
	$c_1$	$c_2$	$c_3$	$c_4$	$c_5$	$c_1$	$c_2$	$c_3$	$c_4$	$c_5$	
2 Min	SPUR-iG (Ours)	<b>33.6±2.1</b>	<b>32.7±2.7</b>	<b>32.1±2.3</b>	<b>32.1±2.2</b>	<b>33.0±2.3</b>	<b>0.94±0.02</b>	<b>0.87±0.03</b>	<b>0.87±0.03</b>	<b>0.87±0.03</b>	<b>0.87±0.03</b>
	Hybrid 2D/3D	32.9±2.1	32.3±2.5	31.4±2.2	31.3±2.3	32.0±2.4	0.93±0.03	0.86±0.03	0.85±0.03	0.86±0.03	0.87±0.03
	LLR	32.0±1.9	31.1±2.2	31.0±1.9	30.8±1.9	30.7±2.0	0.91±0.03	0.83±0.04	0.84±0.03	0.84±0.03	0.83±0.03
1 Min	SPUR-iG (Ours)	<b>30.4±2.3</b>	<b>30.5±2.8</b>	<b>29.7±2.4</b>	<b>29.2±2.7</b>	<b>30.4±2.4</b>	<b>0.89±0.04</b>	<b>0.79±0.04</b>	<b>0.80±0.04</b>	<b>0.80±0.05</b>	<b>0.80±0.04</b>
	Hybrid 2D/3D	29.5±2.3	29.6±2.5	28.9±2.3	28.7±2.5	29.0±2.7	0.87±0.04	0.78±0.04	0.78±0.04	0.78±0.04	0.78±0.04
	LLR	28.2±2.1	27.9±2.2	28.0±2.1	27.8±2.1	27.5±1.9	0.81±0.06	0.69±0.05	0.73±0.04	0.72±0.04	0.70±0.04
30 S	SPUR-iG (Ours)	<b>28.0±2.4</b>	<b>28.5±3.0</b>	<b>27.6±2.6</b>	<b>26.9±2.9</b>	<b>28.8±2.5</b>	<b>0.84±0.06</b>	<b>0.75±0.06</b>	<b>0.75±0.05</b>	<b>0.74±0.05</b>	<b>0.75±0.06</b>
	Hybrid 2D/3D	27.2±2.6	27.9±2.9	26.6±2.7	26.0±3.0	27.3±2.6	0.82±0.06	0.72±0.06	0.72±0.05	0.71±0.05	0.73±0.06
	LLR	24.2±2.2	24.7±2.4	24.0±2.2	23.9±2.3	24.5±2.0	0.72±0.07	0.57±0.06	0.61±0.05	0.60±0.05	0.56±0.05

**TABLE 1** PSNR (left) and SSIM (right) across the five balanced subspace coefficients ( $c_1$ – $c_5$ ). Results are shown for three scan durations: 2 min (top), 1 min (middle), and 30 s (bottom). Metrics are computed on axial brain slices (excluding non-brain slices) and averaged across slices from all test subjects. Values are reported as mean  $\pm$  standard deviation across slices. Bold entries indicate values that are statistically significantly larger than those of the other methods.

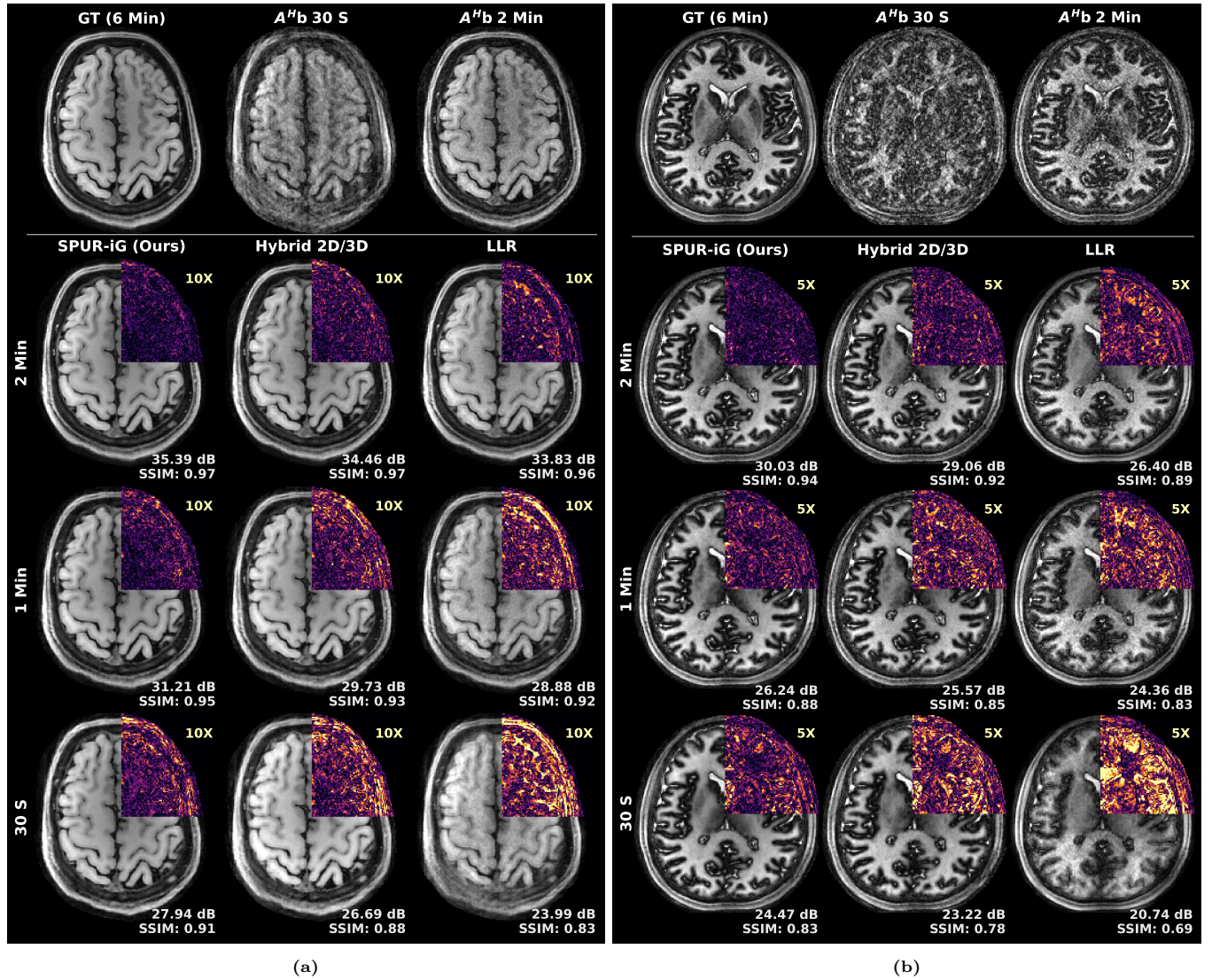


**FIGURE 2** Example reconstructions of the first balanced subspace coefficient (a) and third unbalanced coefficient (b) for two test subjects. The top row shows the 6 min reference (left) and  $\mathcal{A}^H \mathbf{b}$  for the 30 s and 2 min acquisitions (middle and right) as initialization references. Subsequent rows correspond to reconstructions at 2 min, 1 min, and 30 s, with columns comparing our method, the hybrid 2D/3D variant and LLR. PSNR and SSIM are reported in the bottom right of each image. Error maps of the top-right quadrant (magnified  $\times 10$ ) are overlaid to illustrate error levels.

Qualitative results are shown in Fig. 2 for the first balanced and third unbalanced subspace coefficients. These were chosen to display since balanced coefficients generally display flatter contrast, whereas unbalanced coefficients, particularly the third, exhibit higher tissue contrast and reveal finer anatomical details. As scan time decreases, all methods exhibit increased noise, but our approach shows the smallest degradation. For the 30 s scans, both LLR and the hybrid 2D/3D variant produce noisy and over-smoothed reconstructions, whereas our method better preserves fine structure and anatomical details.

### 3.2 | Quantitative Reconstruction

Table. 2 shows the average relative quantitative  $T_1$  and  $T_2$  errors inside the brain (excluding CSF), defined as  $|\mathcal{T}^{\text{GT}} - \hat{\mathcal{T}}|/\mathcal{T}^{\text{GT}}$  for  $\mathcal{T} \in \{T_1, T_2\}$ , where  $\hat{\mathcal{T}}$  denotes the estimated parameter. Across all scan durations, our method achieves lower errors than both baselines. As expected, accuracy decreases with shorter acquisitions, but degradation is less pronounced for our method. Notably, for  $T_1$ , our 30 s scan reconstructions achieved lower average error than LLR reconstructions from a 2 min scan. For  $T_2$ , our approach also provides consistent improvements. Statistical testing confirms that our method outperforms both baselines with  $p < 0.001$  for  $T_1$  and  $T_2$  across all scan durations.

Qualitative results are presented in Fig. 3. For 2 min scans, all methods produce reasonable maps, with ours showing the lowest residual errors. At 30 s, the baseline methods yield overly smoothed maps that lose fine anatomical details, whereas SPUR-iG preserves sharper structures and reduces error.

### 3.3 | Method Ablation

To assess the contribution of individual training stages, we compare the following variants:

1. **Full:** Our complete approach with all three training stages.
2. **GLEAM:** The model after the first two stages, before final fine-tuning.
3. **GLEAM (no PT):** A model trained with GLEAM from scratch, without the pretraining stage. Training time is matched to the combined pretraining and GLEAM training of the **GLEAM** variant for fair comparison.
4. **GLEAM x3 (no PT):** Same as **GLEAM (no PT)**, but trained for three times longer.

To evaluate the effect of unroll iteration conditioning and weight sharing, we further compare:

5. **Full (uncond.):** Full training using an unconditioned model, i.e., without unroll iteration conditioning.
6. **Full (uncond., no WS):** Same as **Full (uncond.)**, but without weight sharing in the GLEAM and fine-tuning stages (resulting in a  $6\times$  increase in parameters).

Fig. 6 shows PSNR and SSIM for the different training variants on 1 min scans (trends are similar for other durations). As can be seen, final fine-tuning provides additional improvements on top of GLEAM, while GLEAM training without pretraining performs poorly. Even when training GLEAM three times longer, performance does not reach that of GLEAM with pretraining.

Iteration conditioning improves performance, and when conditioning is removed, weight sharing decreases performance. Finally, Fig. 7 reports PSNR and SSIM for models trained with a different number of unroll steps, showing that performance improves monotonically and converges around six unroll steps.

### 3.4 | Out-of-distribution generalization

To assess sensitivity to scanner vendor, we acquired data from a single subject on a Siemens 3T system using the same sequence and reconstructed it using the exact same model and setup (which was trained exclusively on GE data). Figures 4 and 5 show the corresponding subspace reconstructions and quantitative maps, which exhibit trends similar to those observed on the in-distribution test set.

### 3.5 | Reconstruction Time

Fig. 8 summarizes reconstruction speedups relative to FISTA LLR. Our method achieves up to  $\times 111$  speedup for the 2 min acquisition and  $\times 51$  for the 30 s acquisition. Compared to iGROG FISTA LLR, the speedups are  $\times 15$  and  $\times 18$  for the 2 min and 30 s cases, respectively. Notably, reconstruction completes in less than 15 s for all acquisition durations. We assume iGROG implicit kernel training is performed during MRF acquisition after calibration data is obtained and therefore does not add to reconstruction time. Speedup decreases for shorter scans because the DC cost scales with the size of the acquired k-space. The hybrid 2D/3D variant is marginally faster than the 3D model (by less than 1 s), but both provide comparable computational efficiency.

Method	2 Min		1 Min		30 S	
	$T_1 \downarrow$	$T_2 \downarrow$	$T_1 \downarrow$	$T_2 \downarrow$	$T_1 \downarrow$	$T_2 \downarrow$
SPUR-iG (Ours)	<b>3.9±2.9</b>	<b>4.8±3.6</b>	<b>5.6±4.1</b>	<b>6.7±4.9</b>	<b>7.1±5.2</b>	<b>8.9±6.5</b>
Hybrid 2D/3D	4.4±3.2	5.1±3.8	6.2±4.5	7.5±5.5	7.7±5.6	9.5±6.9
LLR	7.2±5.0	6.4±4.5	8.2±5.6	8.3±5.9	11.3±7.3	11.1±8.2

**TABLE 2** Relative quantitative  $T_1$  and  $T_2$  errors across methods and scan durations. Values are reported as mean  $\pm$  standard deviation across voxels, averaged over all test subjects, and computed within the brain (excluding CSF). Bold entries indicate values that are statistically significantly lower than those of the other methods.

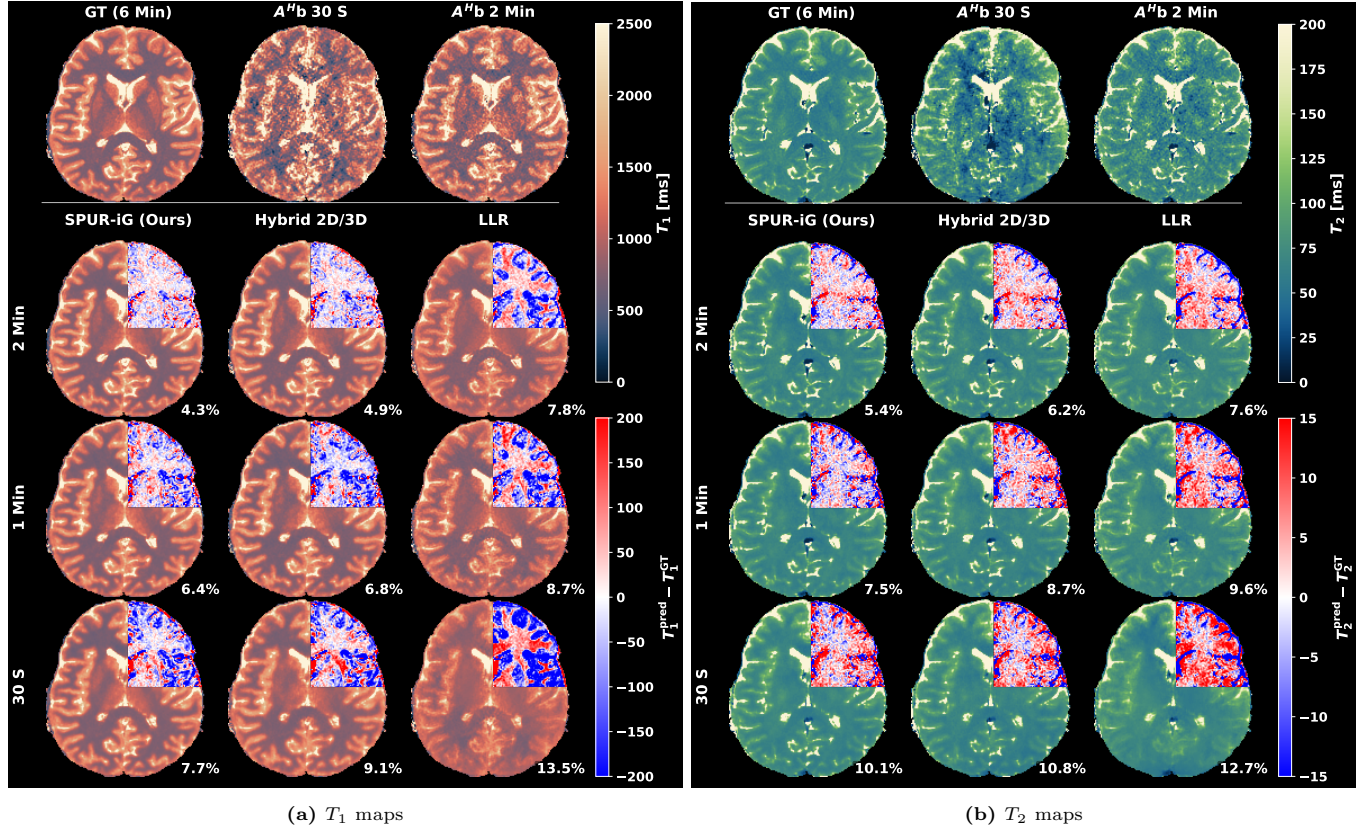


**FIGURE 3** Qualitative examples of reconstructed  $T_1$  (a) and  $T_2$  (b) maps. The first row shows the 6 min reference (left) and maps from  $\mathcal{A}^H\mathbf{b}$  for the 30 s and 2 min acquisitions (middle and right) as references. Subsequent rows present reconstructions at 2 min, 1 min, and 30 s, with columns comparing our method, the hybrid 2D/3D variant, and LLR. Error maps of the top-right quadrant are overlaid on each image. Quantitative colormap (top) and error colormap (bottom) are shown to the right.

## 4 | DISCUSSION

### 4.1 | Quantitative Estimation

With aggressive undersampling, LLR requires stronger regularization to suppress noise, which introduces systematic bias and produces overly smooth maps (Fig. 3, rightmost column). This is most evident at tissue boundaries, where the low-rank assumption does not hold. Although we shift patches during LLR reconstruction to reduce blocking artifacts, the patch-based constraint still couples signals from different tissue types, leading to

biased values at boundaries (e.g., elevated tissue values for WM and reduced values for GM or CSF).

Our learned prior mitigates this effect by replacing patch-based low-rank constraints with a UNet denoiser. Unlike LLR, the UNet produces voxel-wise predictions informed by convolutional receptive fields, allowing it to incorporate spatial context while preserving local tissue differences. In practice, this enables the network to recognize and respect boundaries rather than enforcing a shared representation across them. Residual averaging effects remain, especially at shorter scan durations,

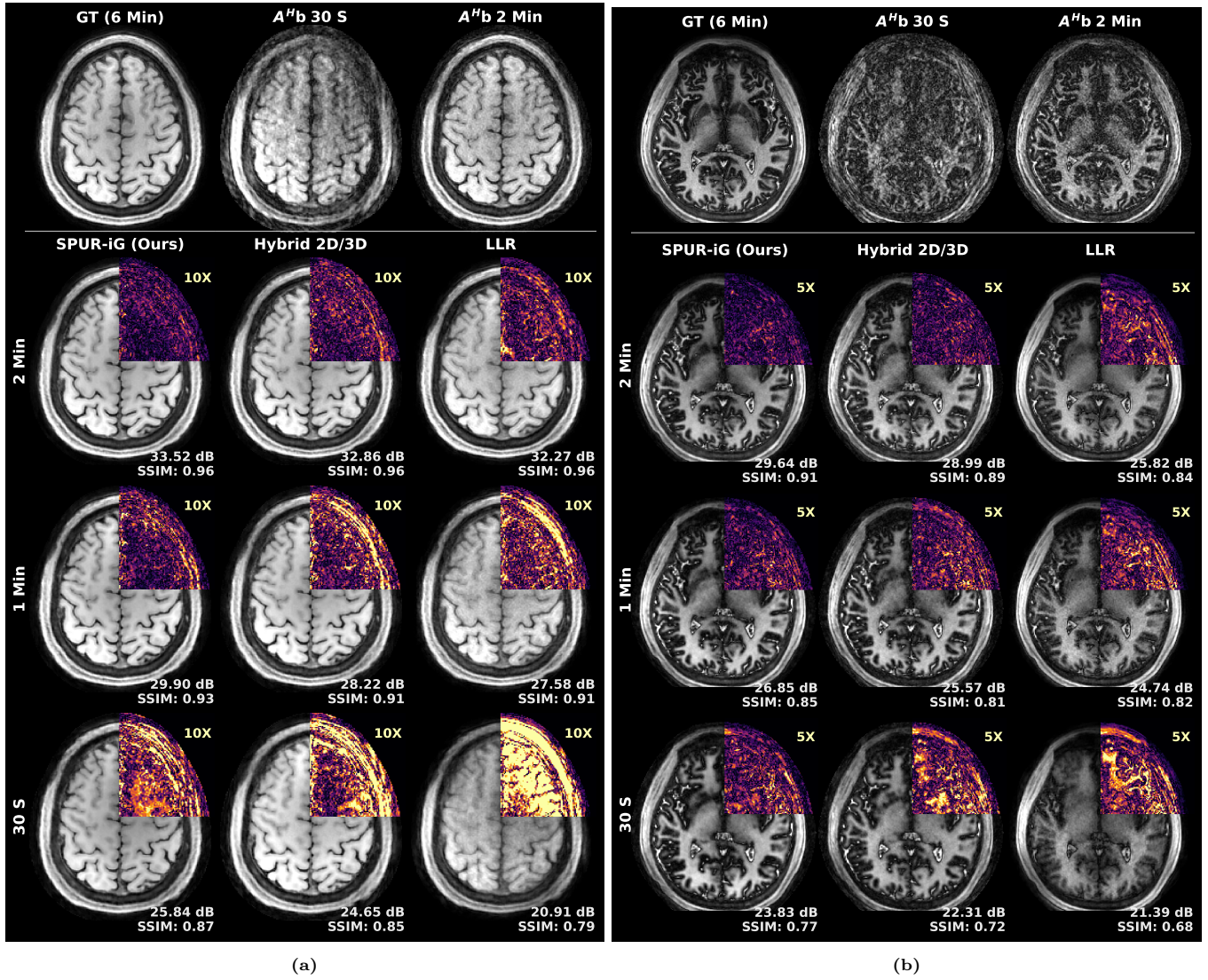


**FIGURE 4** Reconstructions of the first balanced subspace coefficient (a) and the third unbalanced coefficient (b) for two slices from the same subject, scanned on an out-of-distribution scanner vendor. The layout follows Fig. 2.

but they are substantially smaller. The 3D model further reduces this bias by leveraging volumetric context. Most of the remaining error appears in CSF, which is expected since this particular MRF sequence is primarily designed to optimize sensitivity for WM and GM rather than CSF<sup>9</sup>.

Although our training objective is not explicitly designed to optimize tissue quantification, but rather to improve subspace coefficient reconstruction, Table. 2 shows that our method improves quantitative performance, highlighting the benefit of the learned prior. Future work could integrate quantitative parameter estimation directly into the pipeline and jointly optimize for estimation accuracy<sup>24</sup>, or to optimize the learned prior for other downstream applications, such as multi-compartment modeling.

Finally, we use  $B_1$  maps extracted from dummy group scans to correct  $T_2$  bias when performing dictionary fitting. However, as scan duration decreases, the overhead from these groups becomes significant. Future work could integrate calibration-free methods to estimate  $B_1$  maps directly from reconstructed coefficient maps<sup>41</sup>, reducing scan overhead and improving efficiency.

## 4.2 | Coefficient Maps

Coefficient maps preserve richer temporal information than  $T_1/T_2$  maps and are important for emerging downstream applications such as multi-compartment modeling and clinical contrast synthesis. As shown in Table. 1, our method consistently outperforms both baselines in PSNR and SSIM, with performance gaps widening as scan duration decreases. The improvements come from

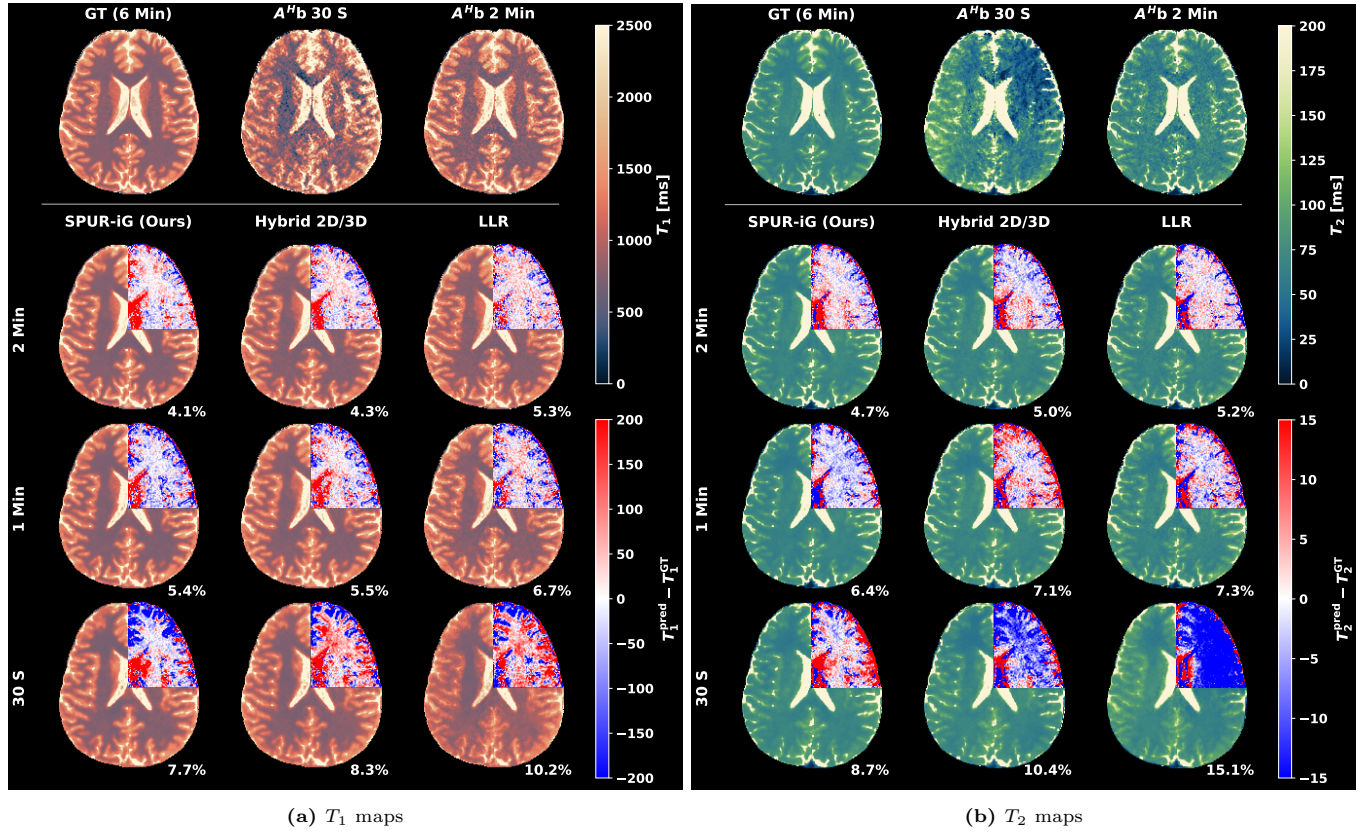


**FIGURE 5** Qualitative examples of reconstructed  $T_1$  (a) and  $T_2$  (b) maps from an out-of-distribution vendor scan. The layout follows Fig. 3.

two factors: the learned prior, which captures more accurate image statistics than hand-crafted regularization, and the 3D UNet architecture, which leverages volumetric correlations across slices for stronger regularization. The proposed training strategy enables training and deployment of such a model, supporting a more complex and accurate representation of image statistics and, consequently, improved reconstructions.

Future work could further improve performance by using optimized spatio-temporal k-space sampling trajectories<sup>24</sup>, which may be especially valuable for very short acquisitions such as 30 s.

### 4.3 | Method Design

Fig. 6 evaluates the impact of different components of our framework.

**Pretraining.** Pretraining is a key element of our approach. By avoiding unrolling and DC, it enables efficient training with extensive data augmentation, which improves generalization and robustness. Without pre-training, GLEAM performs poorly, and even tripling the training time is insufficient to reach comparable performance.

**Final fine-tuning.** Fine-tuning with full unrolling provides a modest but consistent improvement by directly optimizing the final reconstruction loss.

**Iteration conditioning.** Conditioning on the unroll iteration index improves performance over unconditional variants. It simplifies the denoiser’s task by explicitly providing the expected artifact and noise-level distribution, rather than requiring the model to infer these solely from the input. In unconditional training, not sharing weights performs better than sharing, since the model no longer has to infer denoising strength from the input. However, both remain inferior to the conditioned version, which amortizes learning across noise regimes, effectively enlarging the dataset. The cost of conditioning is negligible, adding less than 1% to the model parameters.

**Efficiency.** These design choices enhance performance while achieving low runtime. The learned denoiser is effective at modeling complex distributions, and its inference is efficient, especially on modern GPUs, leading to reduced reconstruction times.

Although the training set consists exclusively of data acquired on a 3T GE system, Figs. 4 and 5 demonstrate that the method generalizes to an out-of-distribution vendor without retraining or fine-tuning,

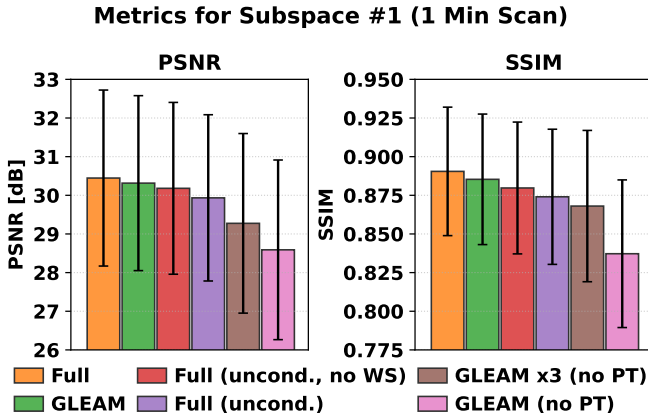


**FIGURE 6** Ablation of training components. PSNR (left) and SSIM (right) for the first subspace coefficient map in 1 min scans. Results are shown for the full approach (Full), training without final fine-tuning (GLEAM), GLEAM without pretraining (GLEAM no PT), GLEAM without pretraining but trained three times longer (GLEAM x3 no PT), full training without unroll iteration conditioning (Full uncond.), and full training without conditioning or weight sharing (Full uncond., no WS). Similar trends are observed across other scan durations and subspace coefficient indices.

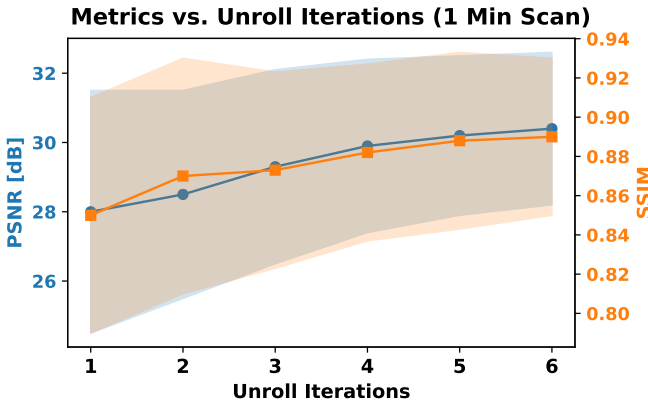


**FIGURE 7** PSNR and SSIM for the first subspace coefficient map in 1 min scans, for models trained with different numbers of unroll iterations. Similar trends are observed across other scan durations and subspace coefficients.

indicating strong cross-vendor robustness. While a modest performance degradation is observed, we expect this gap could be mitigated by incorporating a small amount of out-of-distribution data during training or fine-tuning.

Finally, while demonstrated here for MRF, the proposed 3D unrolled training strategy is generally applicable to other large-scale imaging problems. Applications such as high-resolution structural and dynamic 3D imaging<sup>42</sup> may particularly benefit from its scalability and efficiency.

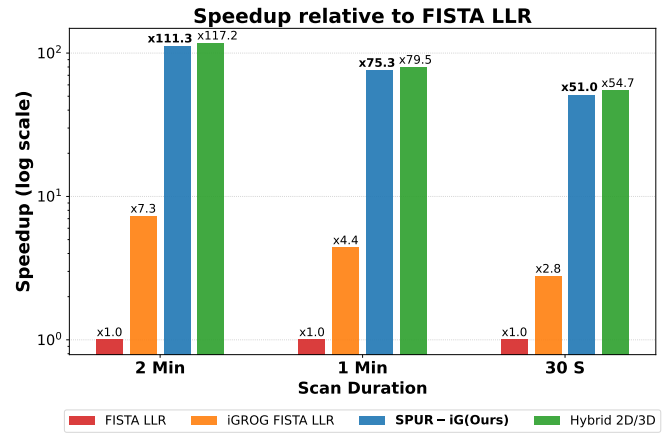


**FIGURE 8** Relative reconstruction speedup compared to FISTA LLR with 40 iterations. The chart compares iGROG with FISTA LLR (40 iterations), our method with six unroll steps, and the 2D unrolled variant with six unroll steps. For methods using iGROG, reconstruction times include gridding but exclude kernel training (which takes less than 25 s), which can be performed in parallel to acquisition. For reference, the reconstruction times (in seconds) for each method and scan duration, from left to right, are: 1758.6, 241.7, 15.8, 15.0, 0 (2 min); 986, 225.3, 13.1, 12.4 (1 min); and 601.7, 217.0, 11.8, 11.0 (30 s). All experiments are performed on a single A6000 GPU.

## 5 | CONCLUSIONS

We propose a fully 3D unrolled MRF reconstruction framework with a staged training strategy that enables large-scale training within practical compute limits. By combining efficient iGROG-based DC with fast 3D UNet-based inference, the method achieves rapid reconstruction while consistently improving quality, supporting acquisitions as short as 30 s and preserving fidelity in both subspace coefficients and quantitative maps

This represents an important step toward enabling short clinical acquisitions with fast reconstructions that can directly produce quantitative maps or synthesize clinical contrasts for routine use. Future work may explore alternative training objectives tailored to downstream applications, such as directly optimizing  $T_1/T_2$  estimation or multi-compartment fitting. Another interesting direction is to extend the staged training strategy to even higher-resolution MRF such as 360  $\mu\text{m}$  isotropic<sup>37</sup>, while keeping computation and memory demands tractable.

## FUNDING INFORMATION

Grant/Award Number: National Institutes of Health R01 EB033206, MH116173 & EB019437.

## REFERENCES

1. Gracién René-Maxime, Maiworm Michelle, Brüche Nadine, et al. How stable is quantitative MRI?—Assessment of intra-and inter-scanner-model reproducibility using identical acquisition sequences and data analysis programs. *Neuroimage*. 2020;207:116364.
2. Mezer Aviv, Yeatman Jason D, Stikov Nikola, et al. Quantifying the local tissue volume and composition in individual brains with magnetic resonance imaging. *Nature medicine*. 2013;19(12):1667–1672.
3. Yablonski Maya, Zhou Zihan, Cao Xiaozhi, et al. Fast and reliable quantitative measures of white matter development with magnetic resonance fingerprinting. *Imaging Neuroscience*. 2025;3:00470.
4. Tang Xiang, Cai Feng, Ding Dong-Xue, Zhang Lu-Lu, Cai Xiu-Ying, Fang Qi. Magnetic resonance imaging relaxation time in Alzheimer’s disease. *Brain research bulletin*. 2018;140:176–189.
5. Luo Xiao, Li Kaicheng, Zeng Qingze, et al. Application of T1/T2-weighted Ratio Mapping to Elucidate the Intracortical Demyelination Process in the Alzheimer’s Disease Continuum. *Frontiers in Neuroscience*. 2019;13.
6. Granziera Cristina, Wuerfel Jens, Barkhof Frederik, et al. Quantitative magnetic resonance imaging towards clinical application in multiple sclerosis. *Brain*. 2021;144(5):1296–1311.
7. Seiler Alexander, Nöth Ulrike, Hok Pavel, et al. Multiparametric quantitative MRI in neurological diseases. *Frontiers in neurology*. 2021;12:640239.
8. Ma Dan, Gulani Vikas, Seiberlich Nicole, et al. Magnetic resonance fingerprinting. *Nature*. 2013;495(7440):187–192.
9. Cao Xiaozhi, Liao Congyu, Iyer Siddharth Srinivasan, et al. Optimized multi-axis spiral projection MR fingerprinting with subspace reconstruction for rapid whole-brain high-isotropic-resolution quantitative imaging. *Magnetic Resonance in Medicine*. 2022;88(1):133–150.
10. Schauman S Sophie, Iyer Siddharth S, Sandino Christopher M, et al. Deep learning initialized compressed sensing (Deli-CS) in volumetric spatio-temporal subspace reconstruction. *Magnetic Resonance Materials in Physics, Biology and Medicine*. 2025;38(2):221–237.
11. Zhao Bo, Setsompop Kawin, Adalsteinsson Elfar, et al. Improved magnetic resonance fingerprinting reconstruction with low-rank and subspace modeling. *Magnetic resonance in medicine*. 2018;79(2):933–942.
12. Assländer Jakob, Cloos Martijn A, Knoll Florian, Sodickson Daniel K, Hennig Jürgen, Lattanzi Riccardo. Low rank alternating direction method of multipliers reconstruction for MR fingerprinting. *Magnetic resonance in medicine*. 2018;79(1):83–96.
13. Liang Zhi-Pei. Spatiotemporal imaging with partially separable functions. In: :988–991 IEEE; 2007.
14. Nagtegaal Martijn, Koken Peter, Amthor Thomas, Doneva Mariya. Fast multi-component analysis using a joint sparsity constraint for MR fingerprinting. *Magnetic resonance in medicine*. 2020;83(2):521–534.
15. Tang Sunli, Fernandez-Granda Carlos, Lannuzel Sylvain, et al. Multicompartment magnetic resonance fingerprinting. *Inverse problems*. 2018;34(9):094005.
16. Yurt Mahmut, Zhou Zihan, Liao Congyu, et al. Unlocking Data-Consistent Synthesis of Clinical Contrasts from Magnetic Resonance Fingerprinting with Semi-Supervised Learning. In: ; 2024. ISMRM Annual Meeting, Singapore.
17. Wang Ke, Doneva Mariya, Meineke Jakob, et al. High-fidelity direct contrast synthesis from magnetic resonance fingerprinting. *Magnetic Resonance in Medicine*. 2023;90(5):2116–2129.
18. Tamir Jonathan I, Uecker Martin, Chen Weitian, et al. T2 shuffling: sharp, multicontrast, volumetric fast spin-echo imaging. *Magnetic resonance in medicine*. 2017;77(1):180–195.
19. Cruz Gastão, Bustin Aurélien, Jaubert Oliver, Schneider Torben, Botnar René M, Prieto Claudia. Sparsity and locally low rank regularization for MR fingerprinting. *Magnetic resonance in medicine*. 2019;81(6):3530–3543.
20. Cai Jian-Feng, Candès Emmanuel J, Shen Zuowei. A singular value thresholding algorithm for matrix completion. *SIAM Journal on optimization*. 2010;20(4):1956–1982.
21. Abraham Daniel, Nishimura Mark, Cao Xiaozhi, Liao Congyu, Setsompop Kawin. Implicit Representation of GRAPPA Kernels for Fast MRI Reconstruction. *arXiv preprint arXiv:2310.10823*. 2023;
22. Abraham Daniel, Nishimura Mark, Cao Xiaozhi, Liao Congyu, Setsompop Kawin. Implicit Neural Representations of GRAPPA Kernels for Rapid Non-Cartesian and Time-Segmented Reconstructions. In: :Abstract 1065; 2024; Singapore.
23. Mildenhall Ben, Srinivasan Pratul P, Tancik Matthew, Barron Jonathan T, Ramamoorthi Ravi, Ng Ren. Nerf: Representing scenes as neural radiance fields for view synthesis. *Communications of the ACM*. 2021;65(1):99–106.
24. Zou Jiaren, Jiang Yun, Kaplan Sydney, Seiberlich Nicole, Cao Yue. Improved Spiral Projection MR Fingerprinting via Memory-Efficient Synergic Optimization of 3D Spiral Trajectory, Image Reconstruction and Parameter Estimation (SOTIP). *IEEE Transactions on Medical Imaging*. 2025;
25. Aggarwal Hemant K, Mani Merry P, Jacob Mathews. MoDL: Model-based deep learning architecture for inverse problems. *IEEE transactions on medical imaging*. 2018;38(2):394–405.
26. Adler Jonas, Öztem Ozan. Learned primal-dual reconstruction. *IEEE transactions on medical imaging*. 2018;37(6):1322–1332.
27. Ozturkler Batu, Sahiner Arda, Ergen Tolga, et al. Gleam: greedy learning for large-scale accelerated MRI reconstruction. *arXiv preprint arXiv:2207.08393*. 2022;
28. Chen Tianqi, Xu Bing, Zhang Chiyuan, Guestrin Carlos. Training deep nets with sublinear memory cost. *arXiv preprint arXiv:1604.06174*. 2016;
29. Beck Amir, Teboulle Marc. A fast iterative shrinkage-thresholding algorithm for linear inverse problems. *SIAM journal on imaging sciences*. 2009;2(1):183–202.

30. Griswold Mark A, Jakob Peter M, Heidemann Robin M, et al. Generalized autocalibrating partially parallel acquisitions (GRAPPA). *Magnetic Resonance in Medicine: An Official Journal of the International Society for Magnetic Resonance in Medicine*. 2002;47(6):1202–1210.
31. Ronneberger Olaf, Fischer Philipp, Brox Thomas. U-net: Convolutional networks for biomedical image segmentation. In: :234–241Springer; 2015.
32. Perez Ethan, Strub Florian, De Vries Harm, Dumoulin Vincent, Courville Aaron. Film: Visual reasoning with a general conditioning layer. In: ; 2018.
33. Ho Jonathan, Jain Ajay, Abbeel Pieter. Denoising diffusion probabilistic models. *Advances in neural information processing systems*. 2020;33:6840–6851.
34. Song Yang, Sohl-Dickstein Jascha, Kingma Diederik P, Kumar Abhishek, Ermon Stefano, Poole Ben. Score-based generative modeling through stochastic differential equations. *arXiv preprint arXiv:2011.13456*. 2020;.
35. Cao Xiaozhi, Ye Huihui, Liao Congyu, Li Qing, He Hongjian, Zhong Jianhui. Fast 3D brain MR fingerprinting based on multi-axis spiral projection trajectory. *Magnetic resonance in medicine*. 2019;82(1):289–301.
36. Cao Xiaozhi, Liao Congyu, Zhu Zheren, et al. Three-dimensional high-isotropic-resolution MR fingerprinting optimized for 0.55 T. *Magnetic resonance in medicine*. 2025;94(1):41–58.
37. Cao Xiaozhi, Beckett Alexander, Liao Congyu, et al. In-vivo quantitative histology using 0.36-mm MR Fingerprinting: technical development. In: ; 2025; Hawaii, United States.
38. Uecker Martin, Lai Peng, Murphy Mark J, et al. ESPIRiT—an eigenvalue approach to autocalibrating parallel MRI: where SENSE meets GRAPPA. *Magnetic resonance in medicine*. 2014;71(3):990–1001.
39. Sled John G, Pike G Bruce. Correction for B1 and B0 variations in quantitative T2 measurements using MRI. *Magnetic Resonance in Medicine: An Official Journal of the International Society for Magnetic Resonance in Medicine*. 2000;43(4):589–593.
40. Fischl Bruce. FreeSurfer. *Neuroimage*. 2012;62(2):774–781.
41. Gao Mengze, Cao Xiaozhi, Abraham Daniel, Zhou Zihan, Setsompop Kawin. Sequence adaptive field-imperfection estimation (SAFE): retrospective estimation and correction of B1+ and B0 inhomogeneities for enhanced MRF quantification. *arXiv preprint arXiv:2312.09488*. 2023;.
42. Ong Frank, Zhu Xucheng, Cheng Joseph Y, et al. Extreme MRI: Large-scale volumetric dynamic imaging from continuous non-gated acquisitions. *Magnetic resonance in medicine*. 2020;84(4):1763–1780.
43. Wu Yuxin, He Kaiming. Group normalization. In: :3–19; 2018.
44. Elfwing Stefan, Uchibe Eiji, Doya Kenji. Sigmoid-weighted linear units for neural network function approximation in reinforcement learning. *Neural networks*. 2018;107:3–11.
45. Hu Jie, Shen Li, Sun Gang. Squeeze-and-excitation networks. In: :7132–7141; 2018.

**How to cite this article:** Urman Y, Nishimura M, Abraham D, Cao X, and Setsompop K (2026), Fully 3D Unrolled Magnetic Resonance Fingerprinting Reconstruction via Staged Pretraining and Implicit Gridding, *Magn. Reson. Med.*.

## APPENDIX

### A | Implementation Details

#### Model

We implemented both 3D and 2D U-Nets with four encoder-decoder levels. Each level contained a residual block consisting of two convolutional layers with kernel size 3, followed by group normalization<sup>43</sup> (8 groups) and SiLU activations<sup>44</sup>. Additionally, a Squeeze-and-Excitation block<sup>45</sup> with reduction factor 16 was applied after each residual block.

Inputs are  $k = 5$  complex subspace volumes, split into  $C = 10$  real/imaginary channels and whitened jointly for zero mean and unit covariance.

Iteration conditioning was implemented by mapping the unroll index  $i$  to sinusoidal embeddings with dimension 48, followed by an MLP generating scale and shift parameters  $(\gamma_i, \beta_i)$ , injected into each block via FiLM-style modulation<sup>32</sup>  $h' = (1 + \gamma_i) \odot h + \beta_i$ .

Unrolled reconstruction is initialized with  $\mathcal{A}^H \mathbf{b} \cdot s$ , where  $s = \|\mathbf{b}\|_2 / \|\mathcal{A} \mathcal{A}^H \mathbf{b}\|_2$  is a scaling factor that aligns the norms of the initialization and the acquired k-space. We found this normalization reduces the number of required unrolled steps.

Training used Adam (initial learning rate  $5 \times 10^{-3}$ , halved after 20 epochs without validation improvement). Pretraining required 4 GPU days, GLEAM training 2 GPU days, and fine-tuning 2 GPU days, all on a single NVIDIA A6000 (48 GB).

#### Pretraining

In pretraining, input types were heuristically matched with iteration indices as

$$\begin{aligned} \mathcal{A}^H \mathbf{b} &\mapsto 1, \\ \boldsymbol{\alpha}_{\text{LLR}}^{\text{30s}} &\mapsto 2, \\ \boldsymbol{\alpha}_{\text{LLR}}^{\text{1min}} &\mapsto 2, \\ \boldsymbol{\alpha}_{\text{LLR}}^{\text{2min}} &\mapsto 3, \\ \boldsymbol{\alpha}_{\text{LLR}}^{\text{6min}} &\mapsto k, \quad k \sim \mathcal{U}[4, 6]. \end{aligned}$$

Here, the highest-quality input  $\boldsymbol{\alpha}_{\text{LLR}}^{\text{6min}}$ , which also serves as the ground truth, is assigned a randomly sampled iteration index  $k$  drawn uniformly from  $\mathcal{U}[4, 6]$ . Data augmentations included random rotations ( $\leq 15^\circ$ ), translations (up to  $\pm 5$  voxels), and scaling in  $[0.98, 1.02]$ . To increase batch diversity, pretraining used randomly cropped  $96^3$  patches with a batch size of 8.

We define a tissue-aware spatially weighted  $L_1$  which we use during pretraining:

$$\mathcal{L}_{\text{spatial}}(\hat{\boldsymbol{\alpha}}, \boldsymbol{\alpha}) = \sum_{v \in \{\text{WM, GM, CSF}\}} \lambda_v \|\hat{\boldsymbol{\alpha}}_v - \boldsymbol{\alpha}_v\|_1, \quad (4)$$

where  $\boldsymbol{\alpha}_v$  and  $\hat{\boldsymbol{\alpha}}_v$  denote the ground truth and estimated coefficient images restricted to tissue class  $v$  (obtained

from the segmentation masks computed from the GT reconstruction). We set  $\lambda_{\text{WM}} = \lambda_{\text{GM}} = 10$  and  $\lambda_{\text{CSF}} = 1$ . This weighting reflects the fact that the acquisition protocol is specifically optimized for sensitivity to WM and GM, and we therefore prioritize accurate estimation in these tissue classes.

#### GLEAM stage

In the GLEAM stage, supervision is applied to all intermediate unroll outputs  $\{\boldsymbol{\alpha}_k\}_{k=1}^K$  using geometrically increasing weights, such that the highest weight is assigned to the final output at step  $K$ . Additionally, we augment the  $L_1$  loss with a multi-scale structural similarity (MS-SSIM). The loss is defined as

$$\mathcal{L}_{\text{GLEAM}} = \sum_{k=1}^K \lambda_k \mathcal{L}_{\text{spatial}}(\boldsymbol{\alpha}_k, \boldsymbol{\alpha}_{\text{gt}}) \quad (5)$$

$$+ \lambda_{\text{SSIM}} \mathcal{L}_{\text{MS-SSIM}}(\boldsymbol{\alpha}_K, \boldsymbol{\alpha}_{\text{gt}}), \quad (6)$$

where  $\boldsymbol{\alpha}_{\text{gt}}$  denotes the ground truth, and  $\{\lambda_k\}$  follow a geometric progression with  $\lambda_K = 10\lambda_1$ . This weighting scheme encourages progressive refinement across unroll iterations while emphasizing accuracy of the final reconstruction. Due to memory constraints, MS-SSIM is computed on 30 randomly selected axial slices per volume. Here we use full volumes as input with a batch size of 1, hence no stitching logic is required, and employed gradient accumulation with a factor of 4.

#### Fine-tuning

The fine-tuning stage uses the same loss, batch size and gradient accumulation formulation as GLEAM, but supervision is applied only to the final output.

#### LLR Reconstruction

Reconstruction used  $10^3$  patches with random shifts per iteration, and SVD thresholds of  $5 \times 10^{-5}$  (6 min),  $1 \times 10^{-4}$  (2 min, 1 min), and  $1.5 \times 10^{-4}$  (30 s).